Model carbon materials derived from tannin to assess the importance of pore connectivity in supercapacitors

J. Castro-Gutiérrez, N. Díez, M. Sevilla, M.T. Izquierdo, A. Celzard, V. Fierro

Model carbon materials derived from tannin to assess the importance of pore connectivity in supercapacitors

Castro-Gutiérrez, J.[1], Díez, N.[2], Sevilla, M.[2], Izquierdo, M. T.[3]

Celzard, A.[1] and Fierro, V.[1,*]

[1] Université de Lorraine, Institut Jean Lamour, UMR CNRS 7198, 27 Rue Philippe Séguin, 88051 Epinal Cedex 9, France.

[2] Instituto de Ciencia y Tecnología del Carbono (INCAR-CSIC), Francisco Pintado Fe 26, 33011 Oviedo, Spain.

[3] Instituto de Carboquímica (ICB-CSIC), Miguel Luesma Castán 4, E-50018 Zaragoza, Spain.

*Corresponding author: Vanessa Fierro, vanessa.fierro@univ-lorraine.fr

Abstract

A surfactant-water-assisted mechanochemical mesostructuration method is used to produce model carbon materials with a disordered or ordered mesoporous structure (DMCs or OMCs, respectively) from a sustainable precursor, mimosa tannin. These model materials, differing only in their mesoporous structure, allow assessing the importance of the connectivity of the micro-mesopore network on the electrochemical performance of the resultant supercapacitors (SCs). Connectivity is studied through the scanning of hysteresis loops from nitrogen adsorption-desorption isotherms and, contrary to what it is suggested in the literature, order is not always beneficial for the performance of SCs. A thorough review of the open literature and comparison with our electrodes led us to conclude that CO_2-activated DMCs and OMCs are among the best materials reported so far, as they exhibit excellent SC behavior, high-rate capability, and long-term stability in aqueous and organic electrolytes. It is showed that ordered mesopores improve the diffusion of the small-size ions of the aqueous electrolyte and hence favor a better performance at high charging rates, resulting in a 12 % higher capacitance retention at 80 A g^{-1} when compared to that obtained with the disordered materials. However, the more interconnected porosity of the disordered materials allows better diffusion of large-size ions, thus improving the electrochemical performance in the organic electrolyte by 15 % at 40 A g^{-1}.

Highlights

- Ordered and disordered mesoporous carbons of high surface area were produced
- After activation, high-rate capability supercapacitors were obtained from them
- Small-size ions of aqueous electrolyte diffuse better in ordered mesopores
- Large-size ions of organic electrolyte diffuse better in disordered mesopores
- Mesopore connectivity strongly affects electrochemical performances

Keywords: Mesoporous carbons, Pore connectivity, CO_2 activation, Hysteresis scanning, Supercapacitors, Tannin

Word count: 6456

Abbreviations

DMC	Disordered mesoporous carbon
OMC	Ordered mesoporous carbon
SC	Supercapacitor
SWAMM	Surfactant-water-assisted mechanochemical mesostructuration
PSD	Pore size distribution
2D-NLDFT HS	2D Non-local density functional theory for heterogeneous surface
CV	Cyclic voltammetry
GCD	Galvanostatic charge-discharge
EIS	Electrochemical impedance spectroscopy
EDR	Equivalent distributed resistance

Nomenclature

A*t*-DMC	Disordered mesoporous carbon activated during *t* minutes
A*t*-OMC	Ordered mesoporous carbon activated during *t* minutes
BO	Burn-off [%]
A_{BET}	Area calculated using the Brunauer–Emmett–Teller theory [$m^2\ g^{-1}$]
S_{NLDFT}	Surface area calculated by applying the 2D-NLDF HS theory [$m^2\ g^{-1}$]
$V_{u\mu}$	Ultramicropore volume [$cm^3\ g^{-1}$]
$V_{s\mu}$	Supermicropore volume [$cm^3\ g^{-1}$]
V_{meso}	Mesopore volume [$cm^3\ g^{-1}$]
p/p_0	Relative pressure
$(p/p_0)_{des}$	Starting relative pressure of the scanned desorption branches
w	Pore width [nm]
w_c	Critical pore width [nm]
$w_{av,2-5nm}$	Average pore width of mesopores in the 2 – 5 nm range [nm]
$w_{av,>5nm}$	Average pore width of mesopores in the 5 – 50 nm range [nm]
$w_{av,meso}$	Average mesopore width [nm]
$V_{2-5\,nm}$	Mesopore volume in the 2 – 5 nm range [$cm^3\ g^{-1}$]
$V_{>5\,nm}$	Mesopore volume in the 5 – 50 nm range [$cm^3\ g^{-1}$]
C_{cell}	Specific cell capacitance [$F\ g^{-1}$]
C_{ret}	Capacitance retention [%]
I	Applied current [$A\ g^{-1}$]
E	Specific energy [$Wh\ kg^{-1}$]
P	Specific power [$W\ kg^{-1}$]
Z_r	Real part of the complex impedance [Ω]
Z_i	Imaginary part of the complex impedance [Ω]

1. Introduction

The depletion of fossil fuel reserves as well as the increasing global warming impose a transition to energy-related technologies that respect the environment. The research for greener technologies is not only applicable to the energy source but also to all the devices and materials involved in the energy consumption chain, *i.e.*, storage, transport, and processing. Mechanochemical synthesis methods have proven to be suitable for the production of a wide variety of materials such as ordered mesoporous polymers, silica composites, and ordered mesoporous carbons, among others [1-6]. Herein, the focus is made on carbon electrodes prepared by a fast and eco-friendly surfactant-water-assisted mechanochemical mesostructuration (SWAMM) method using mimosa tannin as carbon precursor. These materials can be considered as model carbons because their pore mesostructure can be tailored to obtain either ordered or disordered mesoporous carbons, OMCs or DMCs, respectively, while retaining similar textural properties, such as surface area and pore volume [7].

Interest in supercapacitors (SCs) has increased as these devices close the gap between conventional capacitors and batteries in terms of stored energy *vs* power performance [8]. SCs store energy by an accumulation of charges at the electrolyte-electrode interface, thus high surface area materials are required for their fabrication. This surface needs to be available for the electrolyte ions; hence, the importance of adapting the size of the pores to that of the ions of the selected electrolyte to increase accessibility and fully occupy the charge storage sites. Studies reported that a hierarchical structure connecting the micro-, meso- and macroporosity (pore size < 2 nm, between 2 and 50 nm, and > 50 nm, respectively) improves the diffusion in the material, thus enhancing the SCs performance, in particular at high charging rates [9–12]. Indeed, it is generally accepted that, in a porous material, micropores provide charge storage sites while mesopores act as channels for ion transport and diffusion, and the macropores serve as an electrolyte reservoir [12]. In addition, it has been hypothesized that ion transfer

and diffusion could be more efficient in an ordered mesopore structure than in a disordered one [13,14]. Therefore, many studies have focused on designing and engineering mesoporous carbons with adjusted size and morphology of mesopores [9,15].

Biomass is widely used as a raw material for laboratory and commercial production of high surface area carbon materials for electrodes in SCs since biomass waste is abundantly available and generally low cost [16–18]. Recent studies have reported the synthesis of activated carbons (ACs) from biomass and biomass-derived molecules as precursors, such as tannic acid and gelatin, and using inorganic salts as activating agents [19,20]. In particular, tannic acid-derived materials exhibited BET areas above 2000 m^2 g^{-1} and porosity in the micropore and narrow mesopore ranges (~2 – 5 nm), both being of disorder nature [20]. When used as electrodes for SCs in aqueous and organic electrolytes, these ACs reached high values of electrode capacitance at a low rate (up to 260 F g^{-1} at 0.2 A g^{-1}) and high rate capabilities (capacitance retention up to 45 % at 80 A g^{-1} in aqueous electrolyte and up to 88 % at 20 A g^{-1} in organic electrolyte). On the other hand, ordered mesoporous carbons (OMCs) have been synthesized to be used as SC electrodes through hard- or soft-templating routes from a variety of precursors of petrochemical (resorcinol, phenol, among others) or biomass (sucrose, lignin, tannin, among others) origin [4,21–24]. In particular, from these biosource precursors, condensed tannins are of great interest as they are naturally occurring polyphenolic molecules that are already extracted at an industrial scale from many plants and trees, such as mimosa, quebracho, or pine [25]. In addition, the polyflavonoids composing condensed tannins are mostly considered non-toxic for low-amount exposure [26] and they are not classified as hazardous substances [27,28]. The reactivity of condensed tannins is similar to that of phenol or resorcinol, turning the former into an adequate ecological and non-toxic alternative carbon precursor to the later of petrochemical origin [29]. Indeed, in our previous study, it was shown that OMCs derived from mimosa tannin and physically activated with CO_2 can be used as SC

electrodes [30]. High rate capability was achieved in aqueous electrolyte, as the activated OMCs exhibited a capacitance retention of 70 % at 80 A g^{-1}.

The electrochemical performances of the materials described above are just a few examples of the many that can be found in the literature. In most cases, the studies focus on the electrochemical performance of materials with different surface areas and porosity properties (pore volume, size, and distribution) having either a disordered structure as in ACs, or an ordered one as in OMCs, but the effect of the mesopore order and pore connectivity is generally disregarded. A study from Li et al. (2019) [31] reported differences between the electrochemical performances in organic electrolyte (TEABF4/ACN) of two KOH-activated mesoporous carbons with cylinder and gyroid geometries. It was found that the gyroid material reached higher values of capacitance that could be ascribed to its more developed microporosity. In addition, electrochemical tests were performed up to moderate charging rates (5 A g^{-1}) where diffusion differences due to the presence of mesopores are less noticeable. A detailed discussion of the effect of order and its connectivity on the SC performances is still needed. Furthermore, direct comparison between published studies to gain more knowledge about the effect of the order remains difficult, since the order cannot be easily isolated from other factors that also influence the SCs performance such as surface area, pore volume, and size, surface chemistry, or even testing conditions. This study thus aims to assess the effect of the order and connectivity of pores on the electrochemical performances of activated mesoporous carbons. After CO_2 activation, the physicochemical properties of activated DMCs synthesized by the SWAMM method [7] were compared to those of the tannin-derived activated OMCs from our previous study carried out under the same conditions [30]. The electrochemical performances of the two model materials, only differing in the mesopore order, were compared when used as electrodes for SCs in aqueous and organic electrolytes. In particular, the scanning of the hysteresis loops allows studying the

connectivity of the pore system and correlating it to the electrochemical performance, an approach that, to the authors' knowledge, has not yet been used as part of the understanding of the SC performance of mesoporous materials.

2. Experimental

2.1. Materials

Mimosa tannin extract was used as carbon precursor due to its phenolic nature since it is mainly composed of flavonoid units (80-82%). It is commercially available under the name Fintan OP and has been kindly provided by the company SilvaChimica (St Michele Mondovi, Italy). Pluronic® F127 was used as pore-directing agent and was purchased from Sigma-Aldrich. Both were used as received.

2.2. Synthesis

The SWAMM method was used to prepare the DMCs, the synthesis of which has already been detailed elsewhere [7]. In short, mimosa tannin (2 g) and Pluronic® F127 (2 g) were milled together in the presence of water (2 g) for 60 min in a planetary milling machine with agate bowl and balls (PM 100, Retsch, at a rotation speed of 500 rpm). The recovered paste-like material was directly submitted to carbonization at 900 °C (heating rate of 1 °C min^{-1}, dwell time of 1 h and natural cooling) under nitrogen flow (100 mL min^{-1}) to obtain the DMC material. The OMC material used for comparison was prepared according to the same procedure by simply modifying the amount of Pluronic® F127 and water used for the synthesis to 0.75 and 1.75 g, respectively.

2.3. Activation

The DMC material was submitted to CO_2 activation following the same procedure as that used for tannin-derived OMCs [30]. The temperature was increased at a heating rate of 5 °C

min^{-1} up to 900 °C under nitrogen flow (100 mL min^{-1}). Once the final temperature was reached, the gas flow was switched to CO_2 (50 mL min^{-1}) for periods ranging from 15 to 60 min. Finally, the samples were left to cool down to room temperature under nitrogen flow. The activated DMCs and OMCs were labeled A*t*-DMC and A*t*-OMC, respectively, where *t* stands for the activation time in minutes. For the A*t*-OMC materials, the activation time ranged from 15 to 120 min.

2.4. Morphology of the mesoporous structure

A JEM – ARM 200F Cold FEG TEM/STEM equipped with a probe and image spherical aberration correctors was used to acquire transmission electron microscopy (TEM) images. Before observation, powdered samples were dispersed in ethanol by low-power sonication, then a drop of the resultant suspension was deposited on a carbon-coated copper TEM grid (200 mesh) and left to dry in air.

2.5. Pore texture analysis

ASAP 2020 and ASAP 2420 (Micromeritics) automatic adsorption devices were used to acquire N_2 and CO_2 adsorption-desorption isotherms (at -196 and 0 °C, respectively). The Microactive® software (provided by Micromeritics) was used to calculate the BET area (A_{BET}) of the materials. Also, the SAIEUS® software (also provided by Micromeritics) was used to apply the 2D non-local density functional theory for heterogeneous surface (2D-NLDFT HS) to N_2 and CO_2 isotherms. The SAIEUS® software allows calculating the pore size distributions (PSDs) as well as the surface area (S_{NLDFT}), the ultramicropore volume ($V_{u\mu}$, pore size < 0.7 nm), the supermicropore volume ($V_{s\mu}$, 0.7 < pore size < 2 nm) and the mesopore volume (V_{meso}, 2 < pore size < 50 nm). The average pore width at different ranges was calculated by:

$$w_{av} = \frac{\sum_i \left(\frac{dV}{dw}\right)_i w_i}{\sum_i \left(\frac{dV}{dw}\right)_i}$$

2.6. Carbon nanostructure

The Raman spectra of as-synthesized (DMC and OMC) and activated samples (A*t*-DMC and A*t*-OMC) were acquired with a Horiba Scientific XploRa Raman spectrometer using a 50× objective and a green laser light (wavelength 535 nm, circularly polarized and filtered at 10% of its nominal power) dispersed using a holographic grating (1200 lines mm^{-1}). Each spectrum is the result of the accumulation of two spectra measured from 800 to 2200 cm^{-1} over 180 s. As a reference, the Raman spectrum of mimosa tannin directly submitted to carbonization (900 °C under N_2 flow) was also acquired.

2.7. Chemical composition

The C, H, N, and S bulk contents were measured by elemental analysis (EA) carried out in an Elementar Vario EL Cube analyzer; the O bulk content was measured independently in a separate column of the same device. The surface chemistry was studied by X-ray Photoelectron Spectroscopy (XPS) performed using an ESCAPlus OMICROM system with an area of analysis of 1.75 x 2.75 mm. The device was equipped with a hemispherical electron energy analyzer and a Mg X-ray source (1253.6 eV, operated at 15 kV and 15 mA). Pass energy of 50 eV was used for survey scans and 20 eV for high-resolution scans. The CASA software was used to treat the C1s and O1s peaks to obtain the atomic content of each element and to identify the different carbon and oxygen functionalities.

2.8. Electrochemical performance

The carbon material under study was mixed with carbon black (Super C65, Timcal) and PTFE (60 wt% suspension in water, Aldrich) in an 85:5:10 weight ratio to prepare a paste from which disc-shaped electrodes were cut for use as electrodes with a carbon load (CL) of ~10

mg cm^{-2}, *i.e.*, similar to that used in commercial devices. Electrodes were impregnated with 1 M H_2SO_4 or 1 M $TEABF_4$ in acetonitrile (ACN) used as aqueous and organic electrolytes, respectively. A two-electrode cell was used to test the electrochemical performance where two electrodes of comparable mass, separated by a porous glass fiber mat, were placed between two current collectors made of gold (with H_2SO_4) or stainless steel (with $TEABF_4$/ACN), and the electrochemical characterization was carried out using a VMP3 electrochemical workstation (Bio-logic).

Cyclic voltammetry (CV) curves were obtained within a potential window of 1 V for the aqueous electrolyte and 2.7 V for the organic electrolyte. The specific capacitance (C_{cell}, F g^{-1}) of the cell as a function of the scan rate was calculated using the following equation:

$$C_{cell} = \frac{\oint IdV}{s\Delta Vm}$$

were I represents the measured current, s the scan rate, ΔV the potential window, and m the mass of active material in the two electrodes.

Galvanostatic charge-discharge (GCD) curves were also used to calculate C_{cell} from the equation:

$$C_{cell} = \frac{I}{(dV/dt)m}$$

were I represents the applied current, based on the mass of active material in one electrode, and dV/dt is the slope of the discharge curve, determined using the upper half of the curve and after removing the potential drop (iR) [32,33]. Then, the specific energy (E, Wh kg^{-1}) and power (P, W kg^{-1}) was calculated through:

$$E = \frac{1}{2}C_{cell}(V_1^2 - V_2^2)$$

$$P = \frac{E}{\Delta t_{12}}$$

were Δt_{12} is the time necessary to discharge the capacitor between the two operating potentials, $V_{1=} V_{max} - iR$, V_2 was considered equal to zero and Δt_{12} to be the time of complete discharge. For evaluating the long-term stability of the assembled SCs, continuous cycling at 5 A g^{-1} and potentiostatic holding tests were carried out in the two electrolytes.

Finally, electrochemical impedance spectroscopy (EIS) measurements were also performed at open-circuit voltage using an AC signal of 10 mV amplitude and a frequency that ranged from 1 mHz to 100 kHz. Nyquist plots were obtained from the values of the real and imaginary parts of the complex impedance (Z_r and Z_i, respectively).

3. Results and discussion

Figure 1 shows the schematic representation of the synthesis process of DMC and OMC materials by the SWAMM method. Figure 2a shows the burn-off (BO) of the DMC and the OMC with the activation time and TEM images of as-synthesized materials, *i.e.*, before activation, are shown in Figure 2c-e. Besides, small-angle XRD measurements and TEM images, in Figure S1, confirmed the ordered nature of the activated OMCs up to a BO of ~80 % [30]. It should be noted that the activation process seems to be more efficient on the DMC because a higher BO was observed for any given activation time. This finding can be attributed to a higher effective residence time of CO_2 within the particles of the DMC. Due to the disordered structure, CO_2 molecules entering a porous DMC particle should indeed follow a longer path to exit than that in an OMC, as shown schematically in Figure 2b. This longer residence time would result in faster and easier development of the porosity, thus requiring shorter activation times than those of the OMCs, as detailed below. This hypothesis is valid as

long as the nanostructure of the non–activated carbons is comparable, which has been confirmed by Raman spectroscopy. Figure S2a shows the Raman spectra of the DMC, the OMC, and the tannin carbonized (without mesostructuration) at the same temperature. These spectra are strictly identical, verifying that there is no difference regarding the nanostructure, which corresponds to that of very poorly crystallized (*i.e.*, highly defective) carbon. Thus, DMC and OMC should have the same reactivity with CO_2, confirming that the higher texture development of DMC at a given activation time is due to the differences in the mesopore connectivity and therefore in the residence time. Furthermore, Raman spectroscopy of the ordered and disordered activated materials revealed that the intensity ratio of the D and G bands increased and the D band narrowed with activation time, as shown in Figure S2b. This suggests that the activation process consumes in priority the most disordered parts of the carbon network, leading on average to an apparent improvement of the short-range order.

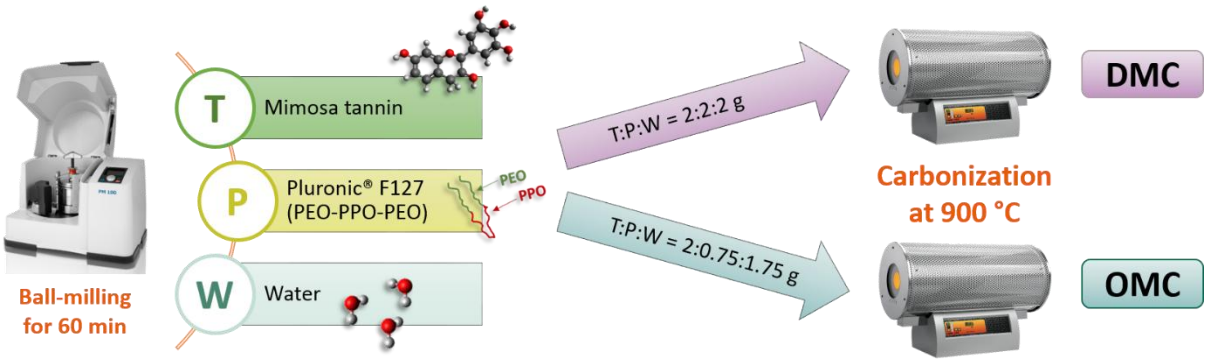

Figure 1. Schematic representation of the synthesis process of disordered and ordered mesoporous carbons (DMC and OMC, respectively) by the SWAMM method.

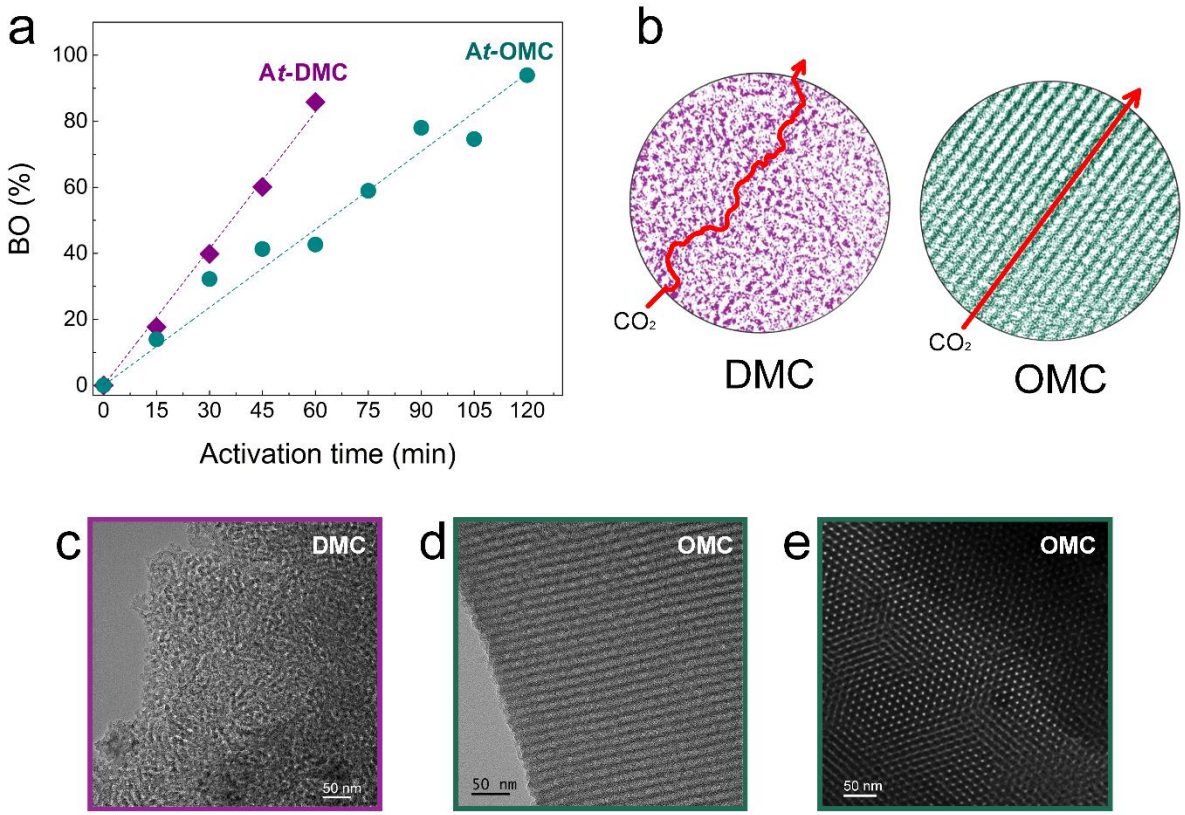

Figure 2. (a) Burn-off (BO) as a function of activation time for the activated ordered and disordered carbons (A*t*-OMC and A*t*-DMC, respectively). (b) Scheme of different diffusion paths within a particle of disordered and ordered mesoporous carbon (DMC and OMC, respectively). TEM images of (c) DMC and (d, e) OMC materials before activation.

3.1. Textural properties

Figure 3a shows the N_2 adsorption-desorption isotherms for the A*t*-DMC series. According to the IUPAC classification [34], the adsorption branches could be identified as a combination of types I and IV, and the desorption branches presented H5 hysteresis loops, resulting from the combination of two H2 loops. The increasing N_2 uptake for $p/p_0 < 0.2$ after activation is due to the development of microporosity while the shape obtained for $p/p_0 > 0.2$ is related to the presence of large mesopores. Indeed, the PSD of the as-synthesized material presented a broad peak centered at ~ 6 nm that extends to pores wider than 10 nm. As expected, the activation resulted in a widening of the mesoporosity (see Figure 3b). In contrast, the OMC

and its activated counterparts showed PSDs with a narrower peak centered at slightly lower pore diameters of ~ 5 nm. This peak increased in height and width, along with the development of the mainly narrow mesoporosity [30] (see Figure 3c, d). Besides, both DMC and OMC materials presented a narrow peak centered at ~0.5 nm, *i.e.*, ultramicropores that progressively broadened with activation time until they extended across the full micropore range. Figure 4 shows that, when comparing the evolution of surface area (S_{NLDFT} and A_{BET}) and pore volume as a function of BO (all calculated values are listed in Table S1), the two series of activated mesoporous carbons followed the same trends with the BO. The values of S_{NLDFT} and A_{BET} of the disordered materials crossed at BO ≈ 40 % due to under- and over-estimations linked to the assumptions made by the BET method when pores less than 0.7 or wider than 1.2 nm, respectively, are involved [35,36]. In any case, the surface area increased with activation up to a maximum value at BO ≈ 80 % (Figure 4a), and the same behavior as that observed for the surface area was followed by the volumes of supermicropores (0.7 < pore size < 2 nm) and mesopores (2 < pore size < 50 nm), $V_{s\mu}$ and V_{meso}, respectively (Figure 4b). On the contrary, the ultramicropore (pore size < 0.7 nm) volume, $V_{u\mu}$, reached a maximum at BO ≈ 20 %, after which it started to decrease due to the widening and merging of pores. Pore widening and merging also caused the observed drop of $V_{s\mu}$ and V_{meso} for BO > 80 %. This similar textural evolution can be explained by the fact that DMC and OMC are derived from the same carbon precursor, *i.e.*, mimosa tannin, which after carbonization gives the same microporous highly defective carbon.

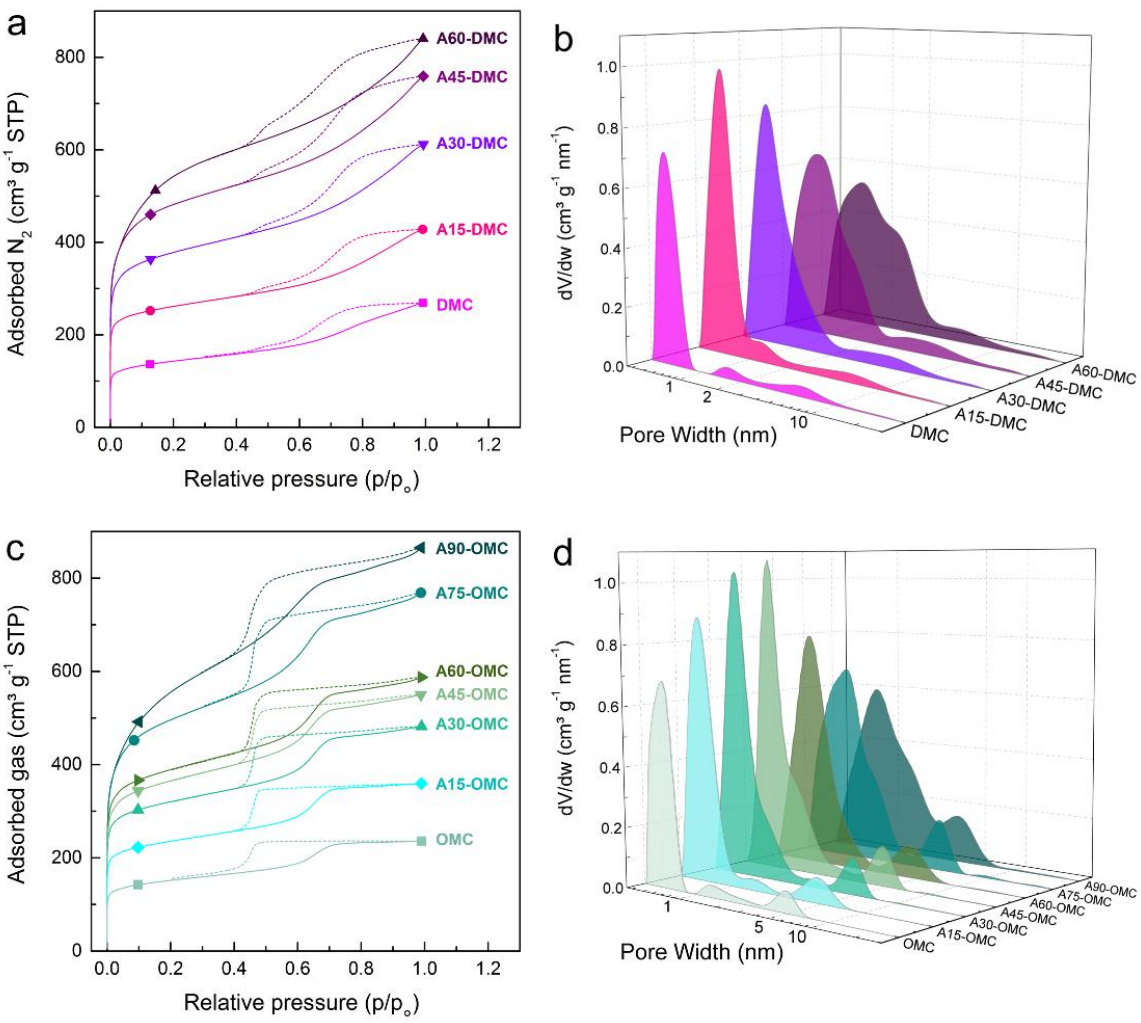

Figure 3. (a, c) N_2 adsorption-desorption isotherms of as-synthesized and activated DMCs and OMCs; (b, d) corresponding PSDs of the same materials, obtained by applying the 2D-NLDFT HS method to N_2 and CO_2 adsorption isotherms (data of A*t*-OMC materials from [30]).

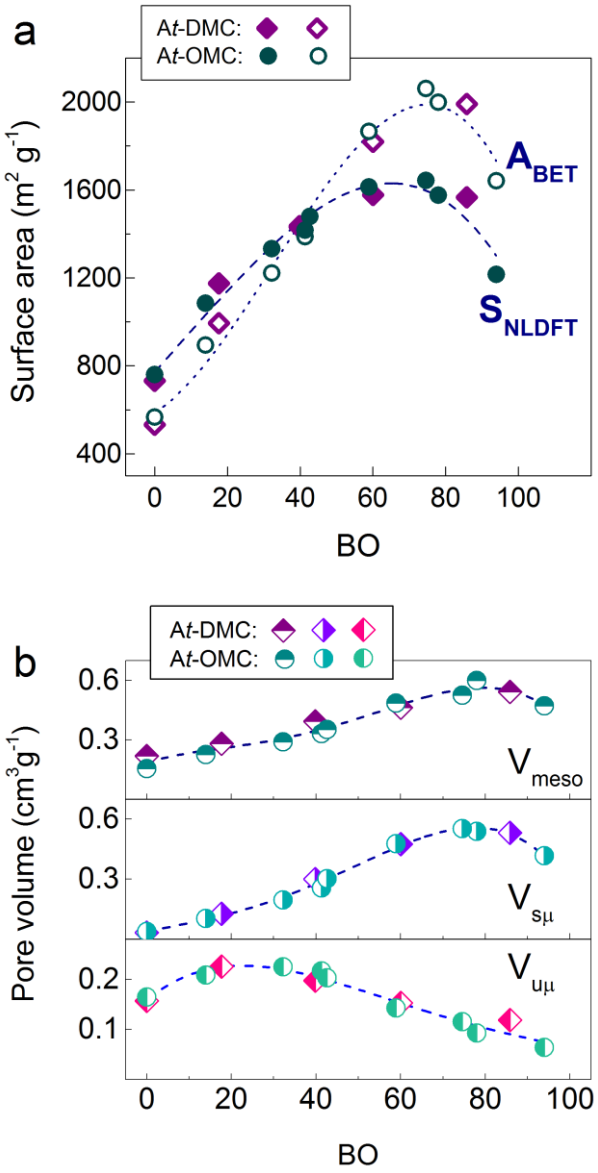

Figure 4. Evolution of (a) 2D-NLDFT HS surface area (S_{NLDFT}) and BET area (A_{BET}), and (b) meso-, supermicro- and ultramicropore volumes (V_{meso}, $V_{s\mu}$ and $V_{u\mu}$, respectively) as a function of burn-off (BO) for the two series of activated DMCs and OMCs (data of A*t*-OMC materials from [30]).

The scanning of the hysteresis loops of the adsorption-desorption isotherms is a useful tool for obtaining more information on the pore network and its connectivity [37,38], and, herein, this technique is used to study the evolution of pore connectivity with activation. It has been reported that in a connected pore system desorption depends on the state of neighboring pores, thus partial filling of the pore network gives rise to desorption curves of different shapes. On

the contrary, when independent pores are present in the material, the onset of desorption is not affected by the state of adjacent pores and the desorption branches obtained from the scanning of the hysteresis loop retain the same shapes. In addition, desorption in H2 loops, associated with the presence of ink-bottle pores, can occur by pore blocking/percolation effects or by cavitation if the neck width, w, is above or below a critical value w_c, respectively [34,39]. Figure 5 shows the scanning of the hysteresis loops of N_2 isotherms that were carried out on as-synthesized and activated materials of the two series studied herein.

Figure 5a, c, e shows the scanning of hysteresis loops of DMC, A15-DMC, and A30-DMC isotherms. The H5 loops observed for the activated DMCs is related to the presence of pores with open and restricted access [34], which can be identified from the behavior of the scanned (or secondary) desorption branches, similar to what had been observed previously for mesostructured zeolites [40]. Figure S3 and a brief explanation of the followed methodology to identify the behavior of the secondary desorption branches of the disordered materials are provided in the Supplementary information. For the first part of the hysteresis loop (*ca.* $p/p_0 > 0.6$), the different shape of the secondary desorption branches with respect to the boundary relates to a network connected through a broad distribution of neck sizes, *i.e.*, desorption occurs due to percolation effects [34,39]. Conversely, on the loop section found for lower relative pressures (*ca.* $p/p_0 < 0.6$), the desorption branches retain the same shapes, a behavior observed in materials with independent or restricted pores. This suggests that desorption is controlled by cavitation, thus indicating that mesopores are connected by micropores or narrow mesopores, such that $w < w_c$ with w_c being 5 nm [37,41]. In addition, by calculating the slope of the tangent line at the starting point of the scanned desorption branches ($(p/p_0)_{des}$), and by plotting it as a function of $(p/p_0)_{des}$ (see Figure 6a), it is possible to observe the changes in the desorption rate and identify these two pore systems. For desorption branches starting at $(p/p_0)_{des} > 0.8$, the desorption rate increased when $(p/$

$p_0)_{des}$ decreased, a faster increase was observed at a higher activation time (*i.e.*, at higher BO) indicating that percolation effects are more important and suggesting an improved pore connectivity after activation. For $(p/p_0)_{des} < 0.8$, where only the narrow mesopores are partially or completely filled, the desorption rate remains constant regardless of the activation time and it decreases as does $(p/p_0)_{des}$, which is an indication of hindered desorption due to restricted access to pores. These analyses allow us to classify the mesopores based on their width as open or restricted, *i.e.*, such that $w > 5$ nm or $2 < w < 5$ nm, respectively. Figure 6b shows the volume of open and restricted pores ($V_{>5\,nm}$ and $V_{2-5\,nm}$, respectively), and Figure 6c displays their average width along with the average pore width of the whole mesoporous system ($w_{av,>5\,nm}$, $w_{av,2-5\,nm}$ and $w_{av,\ meso}$, respectively) for the A*t*-DMC series. It was found that the amount of open pores is greater than that of the restricted ones, that $w_{av,>5\,nm}$ increased from 8 to 9 nm due to pore widening, and that $w_{av,2-5\,nm}$ decreased slightly from 3.5 to 2.8 nm due to the development of narrow mesopores. Finally, since $w_{av,meso}$ remains above the critical pore width ($w_c = 5$ nm), below which access to pores is restricted, it is reasonable to establish that mesopores in the disordered materials constitute a well-connected open network, as schematized in Figure 6d.

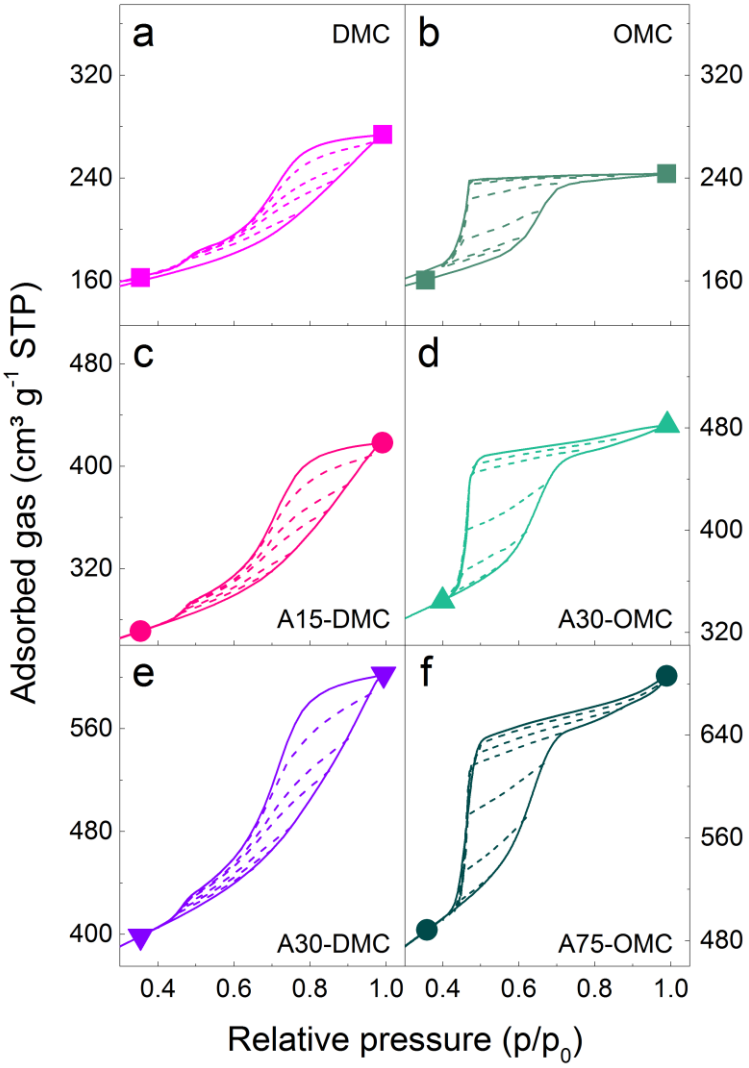

Figure 5. Scanned hysteresis loops of as-synthesized and activated (a, c, e) disordered and (b, d, f) ordered mesoporous carbons. Solid lines represent the boundary adsorption and desorption curves while dotted lines represent the scanned or secondary desorption branches.

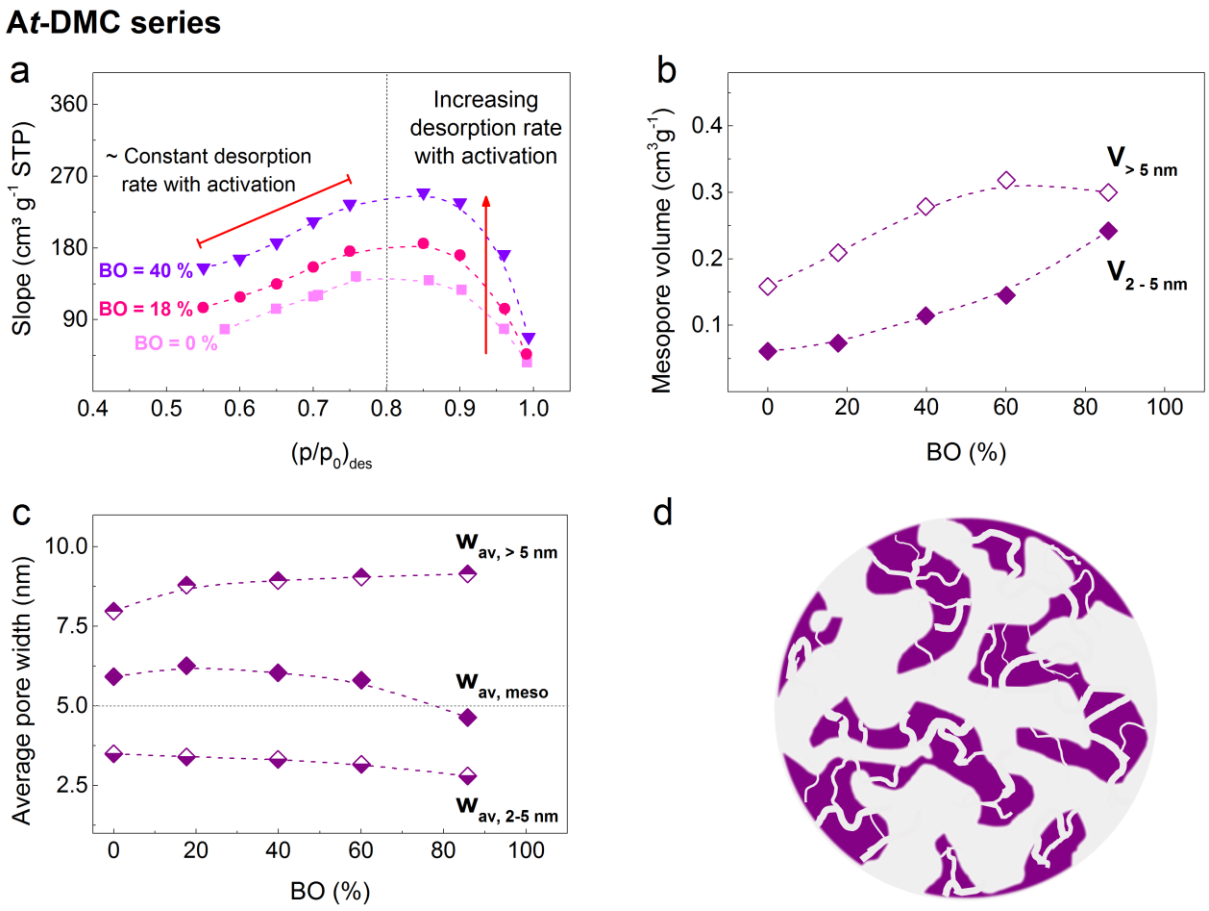

Figure 6. (a) Slope of (a) the tangent line at the starting point ($(p/p_0)_{des}$) of scanned desorption branches as a function of $(p/p_0)_{des}$, for DMC, A15-DMC and A30-DMC samples. (b) Contribution to the mesoporous volume of pores having widths below and above 5 nm ($V_{2-5\,nm}$ and $V_{>5\,nm}$, respectively) and (c) average pore width of mesopores, as well of mesopores in the 2 – 5 nm and 5 – 50 nm ranges ($w_{av,meso}$, $w_{av,2-5\,nm}$ and $w_{av,>5\,nm}$, respectively) for the materials in the A*t*-DMC series. (d) Schematized pore structure of the disordered materials.

The scanning of the hysteresis loop of the OMC, shown in Figure 5b, revealed straight secondary desorption branches with a steep decrease at approximately the same relative pressure. Likewise, A30-OMC and A75-OMC materials exhibited straight scanned desorption branches (Figure 5d, f). Even so, these lines progressively change their slope, Figure 7a displays these changes as a function of $(p/p_0)_{des}$ for the A*t*-OMC series, where again it is

possible to distinguish two trends. For the desorption branches originating from $(p/p_0)_{des} >$ 0.7, the desorption rate is almost constant. Such delayed desorption indicates that wider pores, which are filled last, are isolated or connected only through micropores and/or narrow mesopores ($w < w_c = 5$ nm), which is consistent with the results from our previous study that showed that the channels in the OMC are mainly connected through narrow micropores (pore size ~0.5 nm) [42]. For $(p/p_0)_{des}$ < 0.7, a decreasing desorption rate with a decrease in $(p/p_0)_{des}$ was observed for the OMC. Interestingly, as the BO increased due to activation, the behavior was reversed, *i.e.*, the desorption rate increased as $(p/p_0)_{des}$ decreased. These variations in the desorption rate of partially filled pores suggest the occurrence of percolation in the narrow-mesopore network, which is more important for the A75-OMC. Using the same criteria as for the activated DMCs, the mesopores in the activated OMCs can be classified as open and restricted. Figure 7b, c shows $V_{>5\,nm}$, $V_{2-5\,nm}$, $w_{av,>5\,nm}$, $w_{av,2-5\,nm}$ and $w_{av,\ meso}$ for the ordered materials. In the case of the materials of the A*t*-OMC series, the major contribution to the mesoporous volume comes from the narrow pores, $V_{2-5\,nm}$, which is always higher than $V_{>5\,nm}$, see Figure 7b. Therefore, activation widens the narrow pores connecting the larger channels of the ordered structure, see $w_{av,2-5\,nm}$ in Figure 7c, thereby improving the connectivity. However, the channels of the activated OMCs are still connected through narrow pores ($w < w_c = 5$ nm) and $w_{av,meso}$ is consistently lower than 5 nm; thus, N_2 desorption from mesopores remains mainly restricted by narrow pores, as schematized in Figure 7d.

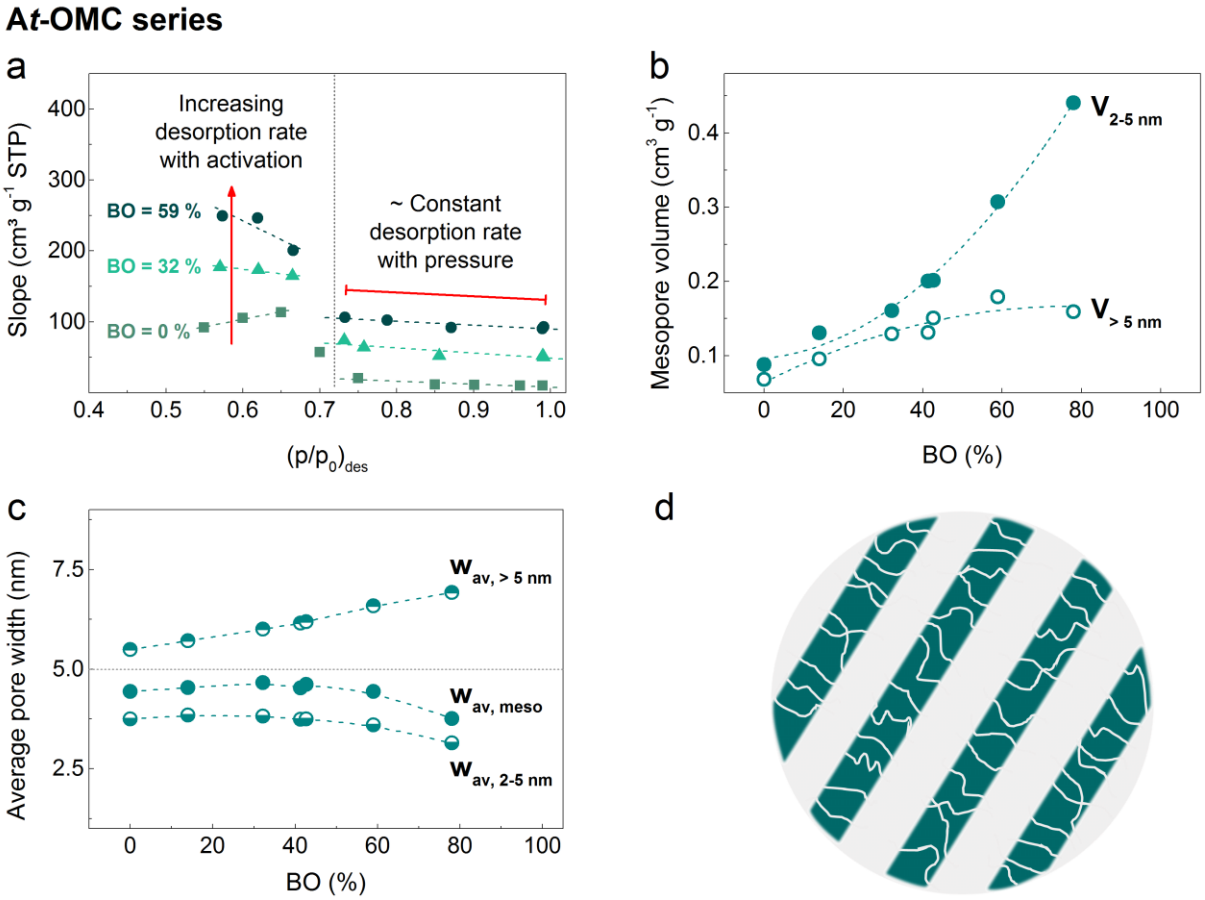

Figure 7. (a) Slope of desorption branches as a function of their starting point $(\mathbf{p/p_0})_{\mathbf{des}}$ for OMC, A30-OMC and A75-OMC samples. (b) Contribution to the mesoporous volume of pores having widths below and above 5 nm ($\mathbf{V_{2-5\ nm}}$ and $\mathbf{V}_{>5\ nm}$, respectively) and (c) average pore width of mesopores, as well of mesopores in the 2 – 5 nm and 5 – 50 nm ranges ($\mathbf{w_{av,meso}}$, $\mathbf{w_{av,2-5\ nm}}$ and $\mathbf{w}_{\mathbf{av,}>5\ nm}$, respectively) for the materials in the At-OMC series. (d) Schematized pore structure of the ordered materials.

3.2. Surface and bulk composition

Figure 8 shows the oxygen (O) content of the materials determined by elemental analysis (EA) and by X-ray photoelectron spectroscopy (XPS); the full EA results are reported in Table S2. In general, a sharp decrease in the O content was produced when materials were slightly activated (BO < 20 %). Additional activation resulted in an augmentation in the O content for both the disordered and ordered materials. Besides, the EA revealed that the

amount of O in the bulk is consistently higher for activated DMCs than for the ordered ones, see Figure 8a; yet, there is a parallel evolution of the O content for the two series of materials, as this difference remains ~4 % for a given value of BO. Besides, as shown in Figure 8b, the O content at the surface remained roughly the same for the two series of materials, following the same trend as the BO increases. This similar behavior of the surface O content suggests that both materials, DMC and OMC, have a similar reactivity towards CO_2 regardless of the differences found in the bulk, again implying that the faster development of porosity properties observed in the A*t*-DMC series is due to longer diffusion paths within its particles.

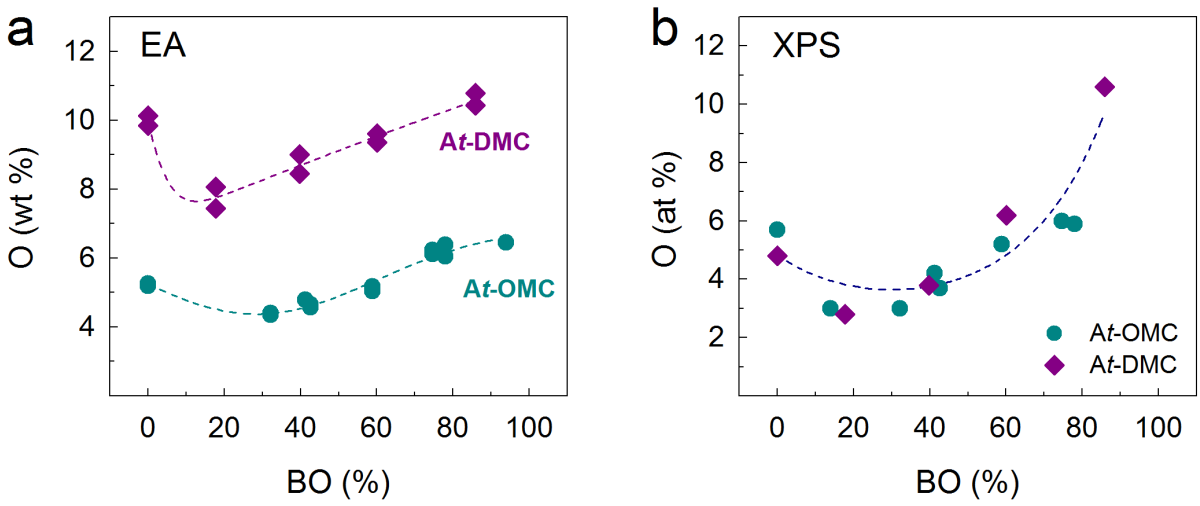

Figure 8. Oxygen content of the two series of activated materials, A*t*-DMCs and A*t*-OMCs, measured (a) by elemental analysis (EA) and (b) by X-ray photoelectron spectroscopy (XPS) (data of A*t*-OMC materials from [30]).

Nonetheless, some differences were found on the relative contributions of surface functional groups for each series when compared as a function of activation time, see Figure S4a,b. The XPS spectra of the A*t*-DMC and A*t*-OMC samples are shown in Figure S5 and Figure S6, respectively, and the complete assignment of peaks and the relative contributions of the

functional groups are listed in Table S3. In the activated DMCs, quinone- and carbonyl-type functionalities (OI) increased up to 45 % for A45-DMC and decreased drastically to ~20 % after 60 min of activation. Meanwhile, for the activated OMCs, the highest OI contribution was found for A30-OMC (36 %), but for t > 30 min, this contribution remained close to 30 %. The contribution of carboxylic groups (OIII) increased considerably with activation time, from 7 to 20 %, for the disordered materials, whereas it increased moderately for the ordered carbons, going from 7 to 11%. Finally, the greatest contribution to O functionalities in both series of activated carbons comes from phenolic groups (OII) due to the polyphenolic nature of the precursor. The presence of certain groups on the surface of carbon materials can contribute to the performances of supercapacitors when using aqueous electrolytes. Especially, OI contributions are reported to be among the most electrochemically active groups that can lead to pseudocapacitance contributions, whereas the high polarity of OIII groups might hinder the diffusion of ions [17].

3.3. Selection of samples for comparison

Based on the characterization carried out on the activated materials, a sample from each series was chosen to study the effect of mesopore order on the electrochemical performance. Figure 9a shows the N_2 and CO_2 adsorption-desorption isotherms, and Figure 9b displays the PSDs and the cumulated volumes of the selected samples, A45-DMC and A75-OMC. It is shown that the textural properties of the two samples are practically the same except for the mesopore order and a wider PSD in the mesopore range for the disordered sample.

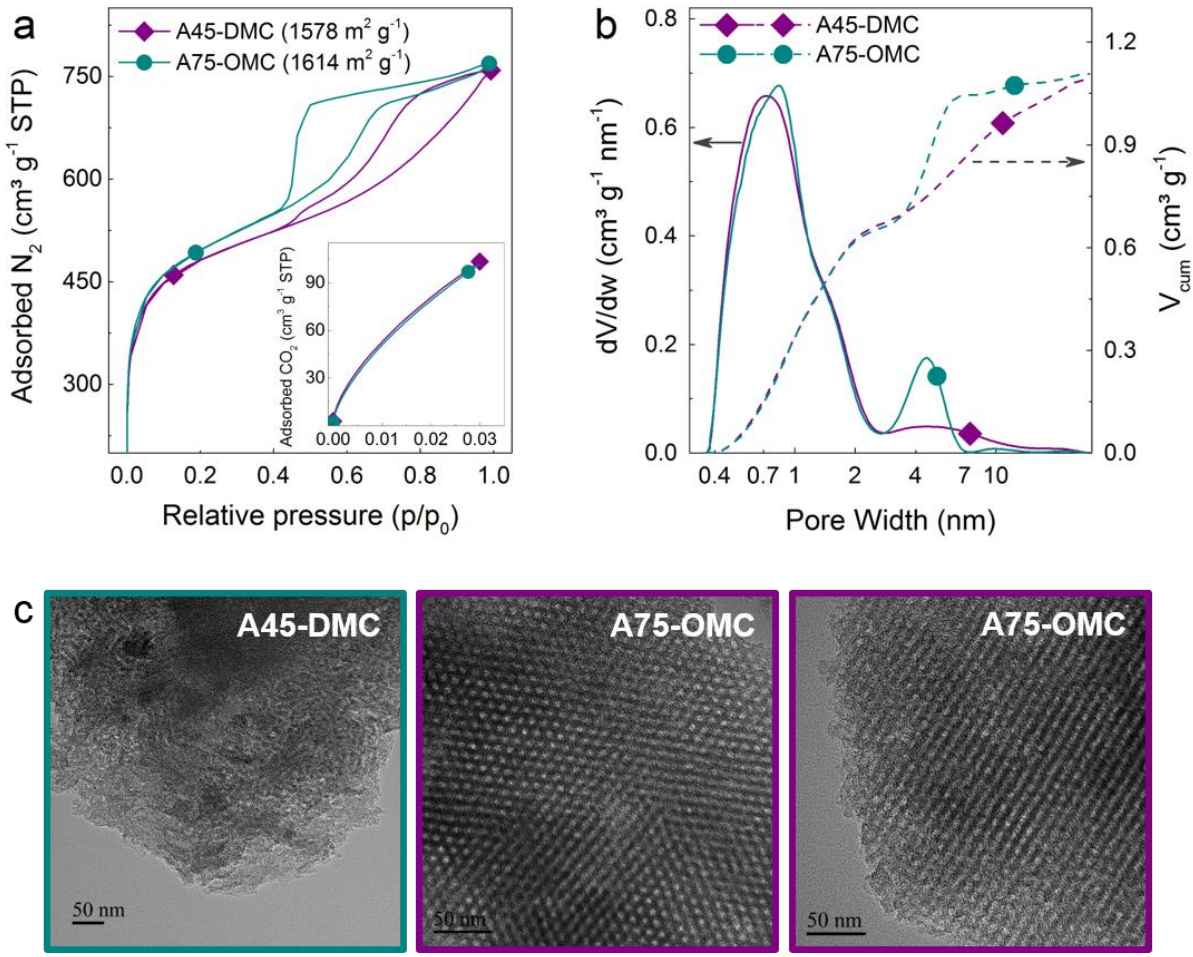

Figure 9. Comparison of the textural properties of A45-DMC and A75-OMC samples: (a) N_2 and (inset) CO_2 isotherms and (b) pore size distributions, in differential (dV/dw, solid lines) and cumulative pore volume (V_{cum}, dashed lines) forms (data of A75-OMC material from [30]). (c) TEM images of A45-DMC (left) and, transverse (center) and longitudinal (right) views of A75-OMC.

3.4. Electrochemical characterization

Electrodes for SCs were prepared using A45-DMC as detailed in Section 2.8. Cyclic voltammetry (CV), galvanostatic charge-discharge (GCD), and electrochemical impedance spectroscopy (EIS) tests were carried out in aqueous (1 M H_2SO_4) and organic (1 M $TEABF_4$ in acetonitrile (ACN)) electrolytes to evaluate their electrochemical performance and compare it to that of A75-OMC, which has been found to have the best performance among the materials of the A*t*-OMC series [30].

In the aqueous electrolyte, Figure 10a shows that A45-DMC, like A75-OMC, presents quasi-rectangular CV curves at a low scan rate (5 mV s^{-1}), proof of the ideal supercapacitor behavior of the materials. As the scan rate increases, A75-OMC performs slightly better than A45-DMC, see Figure 10b. Consistently, for the GCD tests, it is observed that as the charge rate increases, the difference of specific cell capacitance, C_{cell}, increases, A75-OMC reaching higher values, see Figure 10c. It is generally accepted that micropore size has a direct influence on the capacitance of the materials when tested as SCs, particularly at low charging rates [43-45]. Indeed, the study on A*t*-OMC materials showed an increase in capacitance normalized by surface area with decreasing pore size at low charging rate (5 mV s^{-1}) [30], in agreement with previous studies on the subject [43–45]. However, herein the compared materials exhibit similar surface areas and microporosity, as shown in Figure 9. Thus, the electrochemical performance at low charging rate is expected to be practically the same for both materials, which was indeed confirmed by the CV and GCD tests. Also note that for low-rate GCD tests, where possible redox reactions have a greater impact on the performance of SCs, the C_{cell} of the two materials is practically the same, suggesting that the differences in their surface chemistry have a negligible contribution to the capacitance. C_{cell} values obtained from GCD curves were used to calculate the specific energy and power (E and P, respectively) of the assembled SCs, and the resultant Ragone-like plot is shown in Figure 10d. A maximum E of 5 Wh kg^{-1} with a P output of 44 W kg^{-1} is found for both materials. Electrochemical impedance spectroscopy (EIS) tests show that A45-DMC has a larger Warburg region in the Nyquist plot, displayed in Figure 10e; this linear region appearing at mid-frequencies is associated with ion diffusion and indicates that ion diffusion is slower for the disordered material, resulting in a higher equivalent distributed resistance (EDR). The higher EDR of A45-DMC could be due to the presence of OIII groups that hinder ion diffusion. However, there is only a ~1 at% difference in O content on the surface of the

materials, including a contribution of 0.4 and 0.5 at% of carboxylic groups (OIII) in A75-OMC and A45-DMC, respectively, which are also those with the highest water affinity and are therefore associated with the hydrophilic properties of the materials [46,47]. Hence, the higher EDR observed for A45-DMC cannot be fully explained by the small differences in surface chemistry. Then, the difference of EDR between A45-DMC and A75-OMC is attributed to the disordered mesostructure in A45-DMC, which leads to longer diffusion paths for the ions (Figure 2b), slightly reducing its performance, especially at high charging rates. The faster diffusion observed for the A75-OMC resulted in a 12 % higher capacitance retention at 80 A g^{-1} compared to that of A45-DMC at the same conditions.

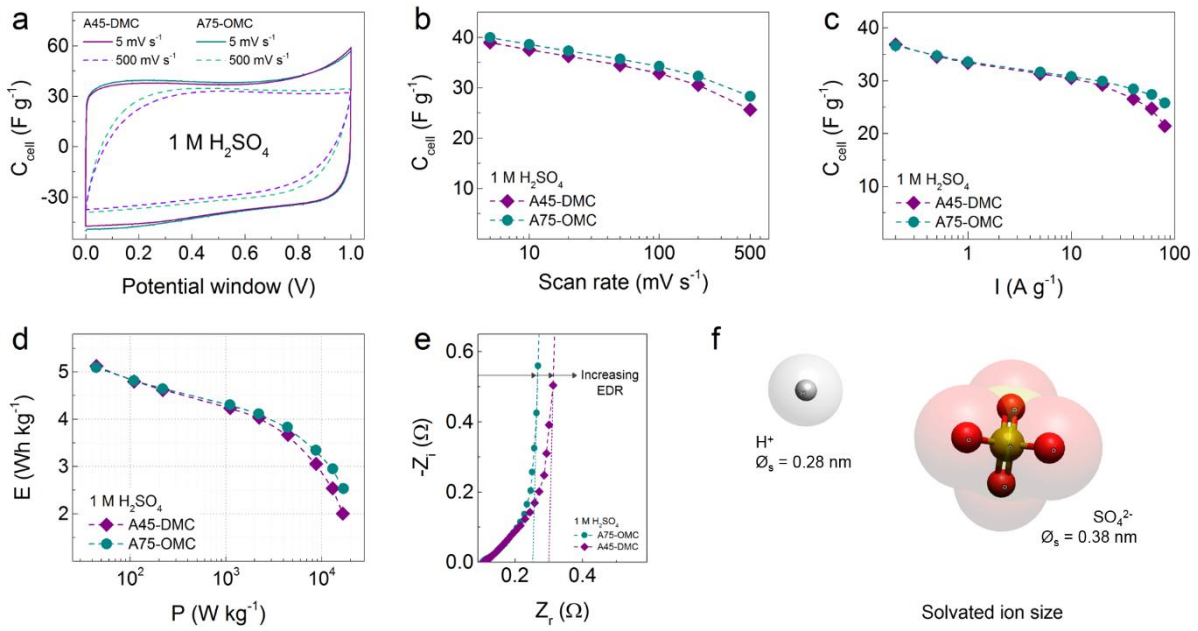

Figure 10. Electrochemical performance of A45-DMC and A75-OMC in aqueous electrolyte (1 M H_2SO_4): (a) CV curves at 5 mV s^{-1}; C_{cell} as a function of (b) scan rate and (c) applied current; (d) Ragone-like plot showing the specific energy and power (*E* and *P*, respectively); and (e) Nyquist plots obtained from EIS measurements (data of A75-OMC material from [30]). (f) Solvated ion size of H_2SO_4 in water [48].

Interestingly, the performance of A45-DMC in organic electrolyte is higher than that of A75-OMC. Figure 11a shows that the two materials present rectangular CV curves at 5 mV s^{-1}, but as the scan rate increases, the C_{cell} values of A75-OMC decrease more rapidly than those of A45-DMC, see Figure 11b. The GCD results are consistent with the aforementioned behavior. In Figure 11c, it is possible to see the change of C_{cell} with the applied current density where, again, A45-DMC outperforms A75-OMC. As expected, in the Ragone-like plot of Figure 11d, similar values of P are found, but A45-DMC reaches higher values of E than A75-OMC, due to the higher C_{cell} of the former material; a maximum E of 29 Wh kg^{-1} with a P of 139 W kg^{-1} was attained by A45-DMC. The better performance of A45-DMC in the organic electrolyte might be due to the different solvated ion sizes, shown in Figure 11f and Figure 11f. Indeed, the ions in $TEABF_4$/ACN are larger than those in H_2SO_4 [48,49], and the scanning of the hysteresis loops has shown that most of the mesopores in A75-OMC are only accessible through narrow mesopores or even micropores, which would reduce the mobility and diffusion of large-sized ions. Despite the larger diffusion path that the disordered structure of A45-DMC represents, its wider PSD in the mesopore range compared to that of A75-OMC (Figure 9) and the well-connected network made up of unrestricted mesopores (Figure 6d) make this material more accessible to $TEABF_4$/ACN ions. From the Nyquist plot obtained from EIS measurements in the organic electrolyte (Figure 11e) it is possible to see that, in this case, the Warburg region is larger for A75-OMC than for A45-DMC indicating that full access to the surface of the material is more difficult for the ordered material due to the narrow connections between mesopores. Consequently, a higher EDR is observed for A75-OMC in comparison with A45-DMC, explaining the better behavior of the latter material due to a favored diffusion of ions at any given charging rate. The more interconnected porosity of A45-DMC allows better diffusion of large-size ions, thus improving the electrochemical

performance in the organic electrolyte by 15 % at 40 A g^{-1} when compared to that attained by the A75-OMC.

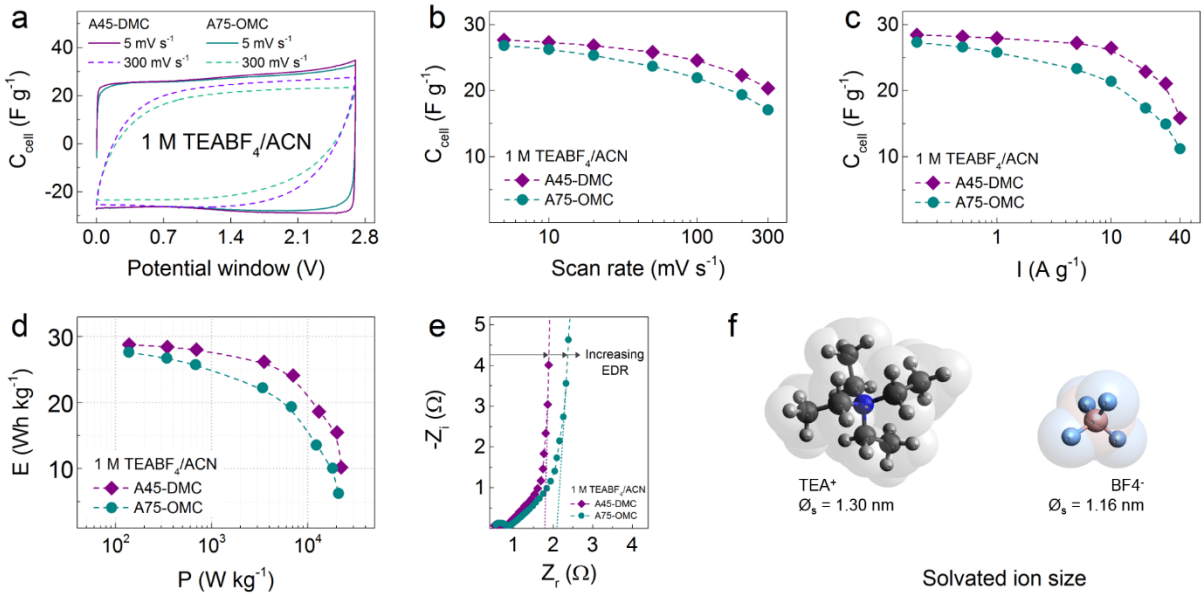

Figure 11. Electrochemical performance of A45-DMC and A75-OMC in organic electrolyte (1 M $TEABF_4$/ACN): (a) CV curves at 5 mV s^{-1}; C_{cell} as a function of (b) scan rate and (c) applied current; (d) Ragone-like plot showing the specific energy and power (*E* and *P*, respectively); and (e) Nyquist plots obtained from EIS measurements (data of A75-OMC material from [30]). (f) Solvated ion size of $TEABF_4$ in acetonitrile [49].

Figure S7 shows the evolution of specific cell capacitance, C_{ret}, of A45-DMC and A75-OMC upon continuous cycling at 5 A g^{-1} and after potentiostatic hold at the maximum voltage (1 V and 2.7 V in aqueous and organic electrolytes, respectively). For both materials, C_{ret} remained above 95 % after 10 000 cycles in the aqueous electrolyte and at 93 % after 8 000 cycles in the organic electrolyte. Moreover, while maintaining the potential at its maximum, C_{ret} again remained above 95 % after 72 h in the aqueous electrolyte and reached 86 % after 72 h in the organic electrolyte. Considering the testing conditions of our study, which are

close to those used in commercial devices (CL of 10 mg cm^{-2}, thickness between 200 to 300 µm), A75-OMC and A45-DMC materials exhibit good electrochemical performance and long-term stability.

3.5. Comparison with the literature

Figure 12a shows the capacitance retention, C_{ret}, vs. applied current of A75-OMC and A45-DMC samples compared to that of similar materials reported in the literature [20,23,31,50–68]. In general, the materials studied here show better rate capabilities in aqueous electrolyte and comparable values in organic electrolyte (see also Table S4 and S5) than those reported in the literature for: mesoporous materials synthesized by soft-templating and followed by a CO_2 [50] or KOH activation process [31], and hard-templating techniques using silica and zeolite templates [23,54–57,61]; carbon nanotubes obtained by chemical vapor deposition of ethylene [60]; carbonized MOFs [65]; graphene oxide derived materials [65–67]; or ACs from different precursors using NaOH, $ZnCl_2$, KOH, $KHCO_3$ or K_2CO_3 as activating agents [20,50–53,58,59,62,63,65,68]. Figure 12b shows a comparison of the values of C_{ret} as a function of A_{BET} at 20 and 10 Ag^{-1} in aqueous and organic electrolyte, respectively. It is possible to observe that A45-DMC and A75-OMC exhibit superior C_{ret} in aqueous electrolyte (> 80 %) and that A45-DMC is among the materials with the highest retention in organic electrolyte (> 90 %); this high rate capability of the tannin-derived mesoporous carbons is an advantage given that supercapacitors are generally needed to supply energy at high power outputs.

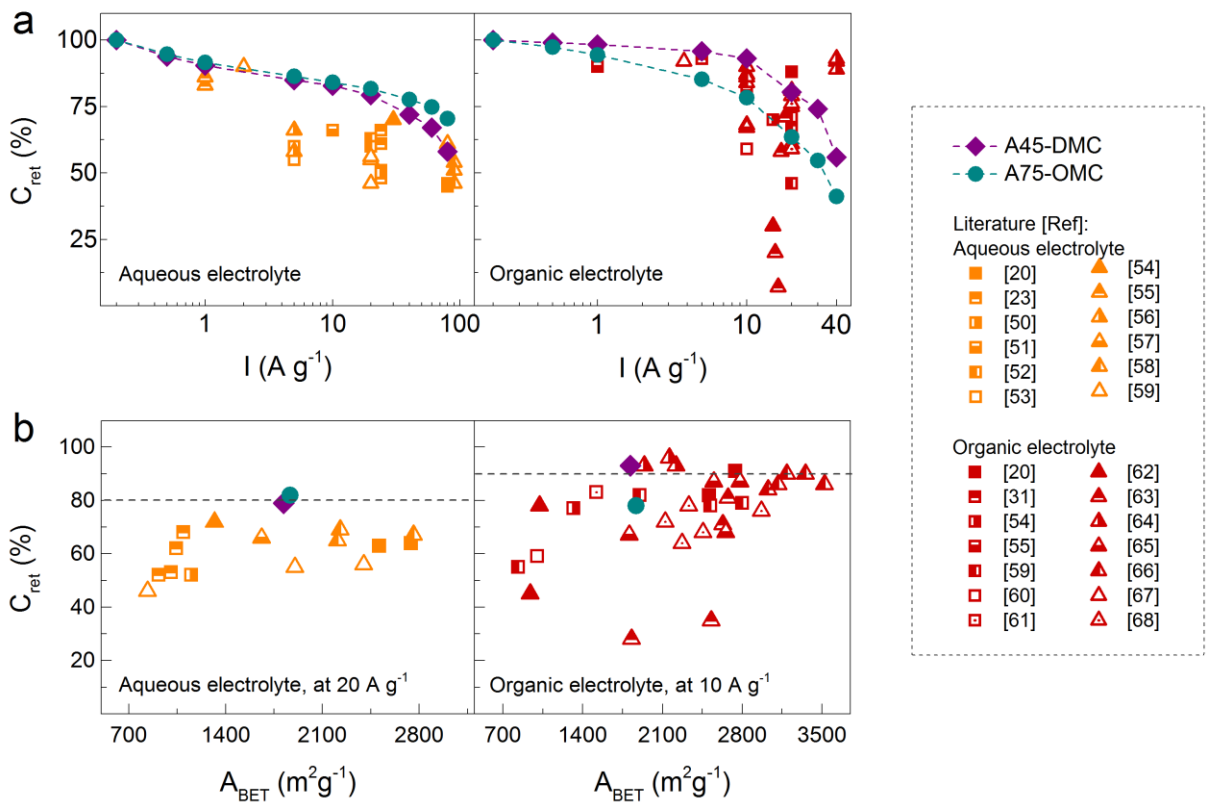

Figure 12. (a) Capacitance retention ($\boldsymbol{C_{ret}}$) as a function of applied current (*I*) for A45-DMC and A75-OMC compared to that of similar materials reported in the literature in aqueous and organic electrolyte (data of A75-OMC material from [30]). (b) $\boldsymbol{C_{ret}}$ as a function of BET area ($\boldsymbol{A_{BET}}$) at 20 and 10 Ag^{-1} in aqueous and organic electrolyte, respectively.

Besides, the methods to produce most of the materials above mentioned, involve multiple steps for the synthesis and etching of templates, pre-treatment of the precursor by freeze-drying, pyrolysis at low temperatures or hydrothermal carbonization, and/or washing of impurities, all of which is time-consuming and usually entails the use of hazardous substances like HF, NaOH or HCl. The synthesis method presented herein requires *ca.* 1.5 days for the production of the activated mesoporous carbons, including the time needed for obtaining the mesophase by mechanosynthesis and performing the carbonization and activation processes. This fast and easy synthesis is a considerable advantage over other complex methods that require not only synthesis times of several days or even weeks, but also drying, aging, and/or

washing steps. On the other side, note also in Figure 12a that the direct pyrolysis of potassium citrate resulted in ACs with higher rate capabilities in organic electrolyte than those of the materials presented herein [64]. The main advantages of the tannin-derived carbons of this study over the potassium citrate-derived ACs are the absence of washing steps (with HCl and water) as part of the production process and the considerably lower price of the precursor. Indeed, mimosa tannin is currently available for ~2 US$ kg^{-1}, which is less than 5 % of the price of potassium citrate [69,70]. Thus, compared to other synthesis processes, the method proposed herein for the production of tannin-derived activated mesoporous carbons could result in lower costs and easier processability in an eventual transition towards large-scale production [71].

4. Conclusion

Model disordered or ordered mesoporous carbons with minor differences in their physicochemical properties were prepared by mechanosynthesis of tannin, followed by carbonization and CO_2 activation. By scanning the hysteresis loop of adsorption-desorption isotherms, it was possible to better understand the connectivity of the mesopore network and relate it to the electrochemical performance of the materials when used as supercapacitor electrodes. To the best authors' knowledge, this approach had not yet being used. This comprehensive analysis showed that, although an ordered structure improves diffusion in aqueous electrolytes, pore network connectivity and pore-ion size matching have an even greater impact in organic electrolytes. A thorough review of the open literature led us to conclude that the tannin-derived activated mesoporous carbons developed herein are a good, environmentally friendly, and inexpensive alternative for use as electrodes in SCs.

Acknowledgments

Jimena Castro-Gutiérrez gratefully acknowledges CONACYT-SENER (601021/438978) for the assigned scholarship to support her PhD studies, resulting in the work presented herein. This study was partly supported by the French PIA project "Lorraine Université d'Excellence", reference ANR-15-IDEX-04-LUE, and the TALiSMAN project, funded by FEDER (2019-000214). Marta Sevilla thanks funding by the Spanish MINECO/FEDER (CTQ2015-63552-R). Special thanks to Philippe Gadonneix for his help in the laboratory and with the EA measurements.

References

[1] F. Liu, Q. Wu, C. Liu, C. Qi, K. Huang, A. Zheng, S. Dai, Ordered Mesoporous Polymers for Biomass Conversions and Cross-Coupling Reactions, ChemSusChem. 9 (2016) 2496–2504. https://doi.org/10.1002/cssc.201600822.

[2] F. Liu, K. Huang, Q. Wu, S. Dai, Solvent‐Free Self‐Assembly to the Synthesis of Nitrogen‐Doped Ordered Mesoporous Polymers for Highly Selective Capture and Conversion of CO_2, Adv. Mater. 29 (2017) 1700445. https://doi.org/10.1002/adma.201700445.

[3] S. Liang, J. Mi, F. Liu, Y. Zheng, Y. Xiao, Y. Cao, L. Jiang, Efficient catalytic elimination of COS and H2S by developing ordered mesoporous carbons with versatile base N sites via a calcination induced self-assembly route, Chemical Engineering Science. 221 (2020) 115714. https://doi.org/10.1016/j.ces.2020.115714.

[4] Q. Wang, Y. Mu, W. Zhang, L. Zhong, Y. Meng, Y. Sun, A facile solvent-free route to synthesize ordered mesoporous carbons, RSC Adv. 4 (2014) 32113–32116. https://doi.org/10.1039/C4RA02743D.

[5] J. Zhu, J. Yang, R. Miao, Z. Yao, X. Zhuang, X. Feng, Nitrogen-enriched, ordered mesoporous carbons for potential electrochemical energy storage, Journal of Materials Chemistry A. 4 (2016) 2286–2292. https://doi.org/10.1039/C5TA09073C.

[6] J. Castro-Gutiérrez, A. Sanchez-Sanchez, J. Ghanbaja, N. Díez, M. Sevilla, A. Celzard, V. Fierro, Synthesis of perfectly ordered mesoporous carbons by water-assisted mechanochemical self-assembly of tannin, Green Chemistry. 20 (2018) 5123–5132. https://doi.org/10.1039/c8gc02295j.

[7] J. Castro-Gutiérrez, A. Sanchez-Sanchez, J. Ghanbaja, N. Díez, M. Sevilla, A. Celzard, V. Fierro, Synthesis of perfectly ordered mesoporous carbons by water-assisted mechanochemical self-assembly of tannin, Green Chemistry. (2018). https://doi.org/10.1039/C8GC02295J.

[8] F. Wang, X. Wu, X. Yuan, Z. Liu, Y. Zhang, L. Fu, Y. Zhu, Q. Zhou, Y. Wu, W. Huang, Latest advances in supercapacitors: from new electrode materials to novel device designs, Chem. Soc. Rev. 46 (2017) 6816–6854. https://doi.org/10.1039/c7cs00205j.

[9] M. Zhang, L. He, T. Shi, R. Zha, Nanocasting and Direct Synthesis Strategies for Mesoporous Carbons as Supercapacitor Electrodes, Chem. Mater. 30 (2018) 7391–7412. https://doi.org/10.1021/acs.chemmater.8b03345.

[10] A. González, E. Goikolea, J.A. Barrena, R. Mysyk, Review on supercapacitors: Technologies and materials, Renewable and Sustainable Energy Reviews. 58 (2016) 1189–1206. https://doi.org/10.1016/j.rser.2015.12.249.

[11] Y. Wang, Y. Song, Y. Xia, Electrochemical capacitors: mechanism, materials, systems, characterization and applications, Chemical Society Reviews. 45 (2016) 5925–5950. https://doi.org/10.1039/C5CS00580A.

[12] F. Beguin, E. Frackowiak, eds., Supercapacitors: Materials, Systems, and Applications, John Wiley & Sons, Ltd, Weinheim, Germany, 2013.

[13] H.-J. Liu, J. Wang, C.-X. Wang, Y.-Y. Xia, Ordered Hierarchical Mesoporous/Microporous Carbon Derived from Mesoporous Titanium-Carbide/Carbon Composites and its Electrochemical Performance in Supercapacitor, Advanced Energy Materials. 1 (2011) 1101–1108. https://doi.org/10.1002/aenm.201100255.

[14] M. Karthik, E. Redondo, E. Goikolea, V. Roddatis, S. Doppiu, R. Mysyk, Effect of Mesopore Ordering in Otherwise Similar Micro/Mesoporous Carbons on the High-Rate Performance of

Electric Double-Layer Capacitors, J. Phys. Chem. C. 118 (2014) 27715–27720. https://doi.org/10.1021/jp508581x.

[15] M. Inagaki, M. Toyoda, Y. Soneda, S. Tsujimura, T. Morishita, Templated mesoporous carbons: Synthesis and applications, Carbon. 107 (2016) 448–473. https://doi.org/10.1016/j.carbon.2016.06.003.

[16] Y. Zhai, Y. Dou, D. Zhao, P.F. Fulvio, R.T. Mayes, S. Dai, Carbon Materials for Chemical Capacitive Energy Storage, Advanced Materials. 23 (2011) 4828–4850. https://doi.org/10.1002/adma.201100984.

[17] M. Sevilla, R. Mokaya, Energy storage applications of activated carbons: supercapacitors and hydrogen storage, Energy Environ. Sci. 7 (2014) 1250–1280. https://doi.org/10.1039/C3EE43525C.

[18] Z. Gao, Y. Zhang, N. Song, X. Li, Biomass-derived renewable carbon materials for electrochemical energy storage, Materials Research Letters. 5 (2017) 69–88. https://doi.org/10.1080/21663831.2016.1250834.

[19] M. Sevilla, N. Diez, G.A. Ferrero, A.B. Fuertes, Sustainable supercapacitor electrodes produced by the activation of biomass with sodium thiosulfate, Energy Storage Materials. 18 (2019) 356–365. https://doi.org/10.1016/j.ensm.2019.01.023.

[20] N. Díez, G.A. Ferrero, M. Sevilla, A.B. Fuertes, A sustainable approach to hierarchically porous carbons from tannic acid and their utilization in supercapacitive energy storage systems, J. Mater. Chem. A. 7 (2019) 14280–14290. https://doi.org/10.1039/C9TA01712G.

[21] S. Lu, Y. Song, K. Guo, X. Chen, J. Xu, L. Zhao, Effect of aqueous electrolytes on the electrochemical behaviors of ordered mesoporous carbon composites after KOH activation as supercapacitors electrodes, Journal of Electroanalytical Chemistry. 818 (2018) 58–67. https://doi.org/10.1016/j.jelechem.2018.04.025.

[22] S. Herou, M.C. Ribadeneyra, R. Madhu, V. Araullo-Peters, A. Jensen, P. Schlee, M. Titirici, Ordered mesoporous carbons from lignin: a new class of biobased electrodes for supercapacitors, Green Chem. 21 (2019) 550–559. https://doi.org/10.1039/C8GC03497D.

[23] A. Sanchez-Sanchez, M.T. Izquierdo, J. Ghanbaja, G. Medjahdi, S. Mathieu, A. Celzard, V. Fierro, Excellent electrochemical performances of nanocast ordered mesoporous carbons based on tannin-related polyphenols as supercapacitor electrodes, Journal of Power Sources. 344 (2017) 15–24. https://doi.org/10.1016/j.jpowsour.2017.01.099.

[24] W. Xing, S.Z. Qiao, R.G. Ding, F. Li, G.Q. Lu, Z.F. Yan, H.M. Cheng, Superior electric double layer capacitors using ordered mesoporous carbons, Carbon. 44 (2006) 216–224. https://doi.org/10.1016/j.carbon.2005.07.029.

[25] P.L. de Hoyos-Martínez, J. Merle, J. Labidi, F. Charrier – El Bouhtoury, Tannins extraction: A key point for their valorization and cleaner production, Journal of Cleaner Production. 206 (2019) 1138–1155. https://doi.org/10.1016/j.jclepro.2018.09.243.

[26] S. Schlienger, A.-L. Graff, A. Celzard, J. Parmentier, Direct synthesis of ordered mesoporous polymer and carbon materials by a biosourced precursor, Green Chem. 14 (2012) 313–316. https://doi.org/10.1039/C2GC16160E.

[27] S. Kim, J. Chen, T. Cheng, A. Gindulyte, J. He, S. He, Q. Li, B.A. Shoemaker, P.A. Thiessen, B. Yu, L. Zaslavsky, J. Zhang, E.E. Bolton, PubChem 2019 update: improved access to chemical data, Nucleic Acids Research. 47 (2018). https://doi.org/10.1093/nar/gky1033.

[28] National Institute for Occupational Safety and Health, NIOSH Pocket Guide to Chemical Hazards, (2018). https://www.cdc.gov/niosh/npg/npgsyn-a.html# (accessed April 24, 2020).

[29] Y. Shirmohammadli, D. Efhamisisi, A. Pizzi, Tannins as a sustainable raw material for green chemistry: A review, Industrial Crops and Products. 126 (2018) 316–332. https://doi.org/10.1016/j.indcrop.2018.10.034.

[30] J. Castro-Gutiérrez, N. Díez, M. Sevilla, M.T. Izquierdo, J. Ghanbaja, A. Celzard, V. Fierro, High-Rate Capability of Supercapacitors Based on Tannin-Derived Ordered Mesoporous Carbons, ACS Sustainable Chem. Eng. 7 (2019) 17627–17635. https://doi.org/10.1021/acssuschemeng.9b03407.

[31] J.-G. Li, Y.-F. Ho, M.M.M. Ahmed, H.-C. Liang, S.-W. Kuo, Mesoporous Carbons Templated by PEO-PCL Block Copolymers as Electrode Materials for Supercapacitors, Chemistry - A European Journal. 25 (2019) 10456–10463. https://doi.org/10.1002/chem.201901724.

[32] M.D. Stoller, R.S. Ruoff, Best practice methods for determining an electrode material's performance for ultracapacitors, Energy & Environmental Science. 3 (2010) 1294. https://doi.org/10.1039/c0ee00074d.

[33] M. Sevilla, G.A. Ferrero, N. Diez, A.B. Fuertes, One-step synthesis of ultra-high surface area nanoporous carbons and their application for electrochemical energy storage, Carbon. 131 (2018) 193–200. https://doi.org/10.1016/j.carbon.2018.02.021.

[34] M. Thommes, K. Kaneko, A.V. Neimark, J.P. Olivier, F. Rodriguez-Reinoso, J. Rouquerol, K.S.W. Sing, Physisorption of gases, with special reference to the evaluation of surface area and pore size distribution (IUPAC Technical Report), Pure and Applied Chemistry. 87 (2015). https://doi.org/10.1515/pac-2014-1117.

[35] S. Brunauer, P.H. Emmett, E. Teller, Adsorption of Gases in Multimolecular Layers, Journal of the American Chemical Society. 60 (1938) 309–319. https://doi.org/10.1021/ja01269a023.

[36] T.A. Centeno, F. Stoeckli, The assessment of surface areas in porous carbons by two model-independent techniques, the DR equation and DFT, Carbon. 48 (2010) 2478–2486. https://doi.org/10.1016/j.carbon.2010.03.020.

[37] K.A. Cychosz, R. Guillet-Nicolas, J. García-Martínez, M. Thommes, Recent advances in the textural characterization of hierarchically structured nanoporous materials, Chemical Society Reviews. 46 (2017) 389–414. https://doi.org/10.1039/C6CS00391E.

[38] R. Cimino, K.A. Cychosz, M. Thommes, A.V. Neimark, Experimental and theoretical studies of scanning adsorption–desorption isotherms, Colloids and Surfaces A: Physicochemical and Engineering Aspects. 437 (2013) 76–89. https://doi.org/10.1016/j.colsurfa.2013.03.025.

[39] K.A. Cychosz, M. Thommes, Progress in the Physisorption Characterization of Nanoporous Gas Storage Materials, Engineering. 4 (2018) 559–566. https://doi.org/10.1016/j.eng.2018.06.001.

[40] J. Garcia-Martinez, C. Xiao, K.A. Cychosz, K. Li, W. Wan, X. Zou, M. Thommes, Evidence of Intracrystalline Mesostructured Porosity in Zeolites by Advanced Gas Sorption, Electron Tomography and Rotation Electron Diffraction, ChemCatChem. 6 (2014) 3110–3115. https://doi.org/10.1002/cctc.201402499.

[41] M. Thommes, K.A. Cychosz, Physical adsorption characterization of nanoporous materials: progress and challenges, Adsorption. 20 (2014) 233–250. https://doi.org/10.1007/s10450-014-9606-z.

[42] J. Castro-Gutiérrez, E. De Oliveira Jardim, R.L.S. Canevesi, J. Silvestre-Albero, M. Kriesten, M. Thommes, A. Celzard, V. Fierro, Molecular sieving of linear and branched C_6 alkanes by tannin-derived carbons, Carbon. 174 (2021) 413–422. https://doi.org/10.1016/j.carbon.2020.12.061.

[43] J. Chmiola, C. Largeot, P.-L. Taberna, P. Simon, Y. Gogotsi, Desolvation of Ions in Subnanometer Pores and Its Effect on Capacitance and Double-Layer Theory, Angewandte Chemie International Edition. 47 (2008) 3392–3395. https://doi.org/10.1002/anie.200704894.

[44] J. Chmiola, G. Yushin, Y. Gogotsi, C. Portet, P. Simon, P.L. Taberna, Anomalous Increase in Carbon Capacitance at Pore Sizes Less Than 1 Nanometer, Science. 313 (2006) 1760–1763. https://doi.org/10.1126/science.1132195.

[45] J. Huang, B.G. Sumpter, V. Meunier, A Universal Model for Nanoporous Carbon Supercapacitors Applicable to Diverse Pore Regimes, Carbon Materials, and Electrolytes, Chemistry - A European Journal. 14 (2008) 6614–6626. https://doi.org/10.1002/chem.200800639.

[46] L. Liu, S. (Johnathan) Tan, T. Horikawa, D.D. Do, D. Nicholson, J. Liu, Water adsorption on carbon - A review, Advances in Colloid and Interface Science. 250 (2017) 64–78. https://doi.org/10.1016/j.cis.2017.10.002.

[47] V.T. Nguyen, T. Horikawa, D.D. Do, D. Nicholson, Water as a potential molecular probe for functional groups on carbon surfaces, Carbon. 67 (2014) 72–78. https://doi.org/10.1016/j.carbon.2013.09.057.

[48] C. Zhong, Y. Deng, W. Hu, J. Qiao, L. Zhang, J. Zhang, A review of electrolyte materials and compositions for electrochemical supercapacitors, Chemical Society Reviews. 44 (2015) 7484–7539. https://doi.org/10.1039/C5CS00303B.

[49] C.-M. Yang, Y.-J. Kim, M. Endo, H. Kanoh, M. Yudasaka, S. Iijima, K. Kaneko, Nanowindow-Regulated Specific Capacitance of Supercapacitor Electrodes of Single-Wall Carbon Nanohorns,

Journal of the American Chemical Society. 129 (2007) 20–21. https://doi.org/10.1021/ja065501k.

[50] A. Sanchez-Sanchez, M.T. Izquierdo, G. Medjahdi, J. Ghanbaja, A. Celzard, V. Fierro, Ordered mesoporous carbons obtained by soft-templating of tannin in mild conditions, Microporous and Mesoporous Materials. 270 (2018) 127–139. https://doi.org/10.1016/j.micromeso.2018.05.017.

[51] A. Elmouwahidi, J. Castelo-Quibén, J.F. Vivo-Vilches, A.F. Pérez-Cadenas, F.J. Maldonado-Hódar, F. Carrasco-Marín, Activated carbons from agricultural waste solvothermally doped with sulphur as electrodes for supercapacitors, Chemical Engineering Journal. 334 (2018) 1835–1841. https://doi.org/10.1016/j.cej.2017.11.141.

[52] Z. Li, L. Zhang, B.S. Amirkhiz, X. Tan, Z. Xu, H. Wang, B.C. Olsen, C.M.B. Holt, D. Mitlin, Carbonized Chicken Eggshell Membranes with 3D Architectures as High-Performance Electrode Materials for Supercapacitors, Advanced Energy Materials. 2 (2012) 431–437. https://doi.org/10.1002/aenm.201100548.

[53] V. Ruiz, C. Blanco, R. Santamaría, J.M. Ramos-Fernández, M. Martínez-Escandell, A. Sepúlveda-Escribano, F. Rodríguez-Reinoso, An activated carbon monolith as an electrode material for supercapacitors, Carbon. 47 (2009) 195–200. https://doi.org/10.1016/j.carbon.2008.09.048.

[54] Q. Li, R. Jiang, Y. Dou, Z. Wu, T. Huang, D. Feng, J. Yang, A. Yu, D. Zhao, Synthesis of mesoporous carbon spheres with a hierarchical pore structure for the electrochemical double-layer capacitor, Carbon. 49 (2011) 1248–1257. https://doi.org/10.1016/j.carbon.2010.11.043.

[55] A.B. Fuertes, G. Lota, T.A. Centeno, E. Frackowiak, Templated mesoporous carbons for supercapacitor application, Electrochimica Acta. 50 (2005) 2799–2805. https://doi.org/10.1016/j.electacta.2004.11.027.

[56] R. Ruiz-Rosas, M.J. Valero-Romero, D. Salinas-Torres, J. Rodríguez-Mirasol, T. Cordero, E. Morallón, D. Cazorla-Amorós, Electrochemical Performance of Hierarchical Porous Carbon Materials Obtained from the Infiltration of Lignin into Zeolite Templates, ChemSusChem. 7 (2014) 1458–1467. https://doi.org/10.1002/cssc.201301408.

[57] G.A. Ferrero, A.B. Fuertes, M. Sevilla, N-doped porous carbon capsules with tunable porosity for high-performance supercapacitors, Journal of Materials Chemistry A. 3 (2015) 2914–2923. https://doi.org/10.1039/C4TA06022A.

[58] M. Sevilla, A.B. Fuertes, A Green Approach to High-Performance Supercapacitor Electrodes: The Chemical Activation of Hydrochar with Potassium Bicarbonate, ChemSusChem. 9 (2016) 1880–1888. https://doi.org/10.1002/cssc.201600426.

[59] G. Lota, T.A. Centeno, E. Frackowiak, F. Stoeckli, Improvement of the structural and chemical properties of a commercial activated carbon for its application in electrochemical capacitors, Electrochimica Acta. 53 (2008) 2210–2216. https://doi.org/10.1016/j.electacta.2007.09.028.

[60] D.N. Futaba, K. Hata, T. Yamada, T. Hiraoka, Y. Hayamizu, Y. Kakudate, O. Tanaike, H. Hatori, M. Yumura, S. Iijima, Shape-engineerable and highly densely packed single-walled carbon nanotubes and their application as super-capacitor electrodes, Nature Materials. 5 (2006) 987–994. https://doi.org/10.1038/nmat1782.

[61] Z. Chen, J. Wen, C. Yan, L. Rice, H. Sohn, M. Shen, M. Cai, B. Dunn, Y. Lu, High-Performance Supercapacitors Based on Hierarchically Porous Graphite Particles, Advanced Energy Materials. 1 (2011) 551–556. https://doi.org/10.1002/aenm.201100114.

[62] T.E. Rufford, D. Hulicova-Jurcakova, E. Fiset, Z. Zhu, G.Q. Lu, Double-layer capacitance of waste coffee ground activated carbons in an organic electrolyte, Electrochemistry Communications. 11 (2009) 974–977. https://doi.org/10.1016/j.elecom.2009.02.038.

[63] B. Xu, F. Wu, D. Mu, L. Dai, G. Cao, H. Zhang, S. Chen, Y. Yang, Activated carbon prepared from PVDC by NaOH activation as electrode materials for high performance EDLCs with non-aqueous electrolyte, International Journal of Hydrogen Energy. 35 (2010) 632–637. https://doi.org/10.1016/j.ijhydene.2009.10.110.

[64] M. Sevilla, A.B. Fuertes, Direct Synthesis of Highly Porous Interconnected Carbon Nanosheets and Their Application as High-Performance Supercapacitors, ACS Nano. 8 (2014) 5069–5078. https://doi.org/10.1021/nn501124h.

[65] S. Gadipelli, C.A. Howard, J. Guo, N.T. Skipper, H. Zhang, P.R. Shearing, D.J.L. Brett, Superior Multifunctional Activity of Nanoporous Carbons with Widely Tunable Porosity: Enhanced

Storage Capacities for Carbon-Dioxide, Hydrogen, Water, and Electric Charge, Adv. Energy Mater. 10 (2020) 1903649. https://doi.org/10.1002/aenm.201903649.

[66] L. Zhang, F. Zhang, X. Yang, G. Long, Y. Wu, T. Zhang, K. Leng, Y. Huang, Y. Ma, A. Yu, Y. Chen, Porous 3D graphene-based bulk materials with exceptional high surface area and excellent conductivity for supercapacitors, Sci Rep. 3 (2013) 1408. https://doi.org/10.1038/srep01408.

[67] Y. Zhu, S. Murali, M.D. Stoller, K.J. Ganesh, W. Cai, P.J. Ferreira, A. Pirkle, R.M. Wallace, K.A. Cychosz, M. Thommes, D. Su, E.A. Stach, R.S. Ruoff, Carbon-Based Supercapacitors Produced by Activation of Graphene, Science. 332 (2011) 1537–1541. https://doi.org/10.1126/science.1200770.

[68] L. Wei, M. Sevilla, A.B. Fuertes, R. Mokaya, G. Yushin, Hydrothermal Carbonization of Abundant Renewable Natural Organic Chemicals for High-Performance Supercapacitor Electrodes, Advanced Energy Materials. 1 (2011) 356–361. https://doi.org/10.1002/aenm.201100019.

[69] V. Fierro, A. Sánchez-Sánchez, A. Celzard, Tannins as Precursors of Supercapacitor Electrodes, in: E. Rincón-Mejía, A. de las Heras (Eds.), Sustainable Energy Technologies, CRC Press, Boca Raton, Florida, USA, 2018: pp. 201–228.

[70] Sigma-Aldrich, Inc., Potassium citrate tribasic monohydrate, Milipore Sigma. (n.d.). https://www.sigmaaldrich.com/catalog/product/sial/25107?lang=en&region=US&cm_sp=Insite-_-caContent_prodMerch_raiOtherymlCtr-_-prodMerch10-2 (accessed May 19, 2020).

[71] C. Schütter, S. Pohlmann, A. Balducci, Industrial Requirements of Materials for Electrical Double Layer Capacitors: Impact on Current and Future Applications, Adv. Energy Mater. 9 (2019) 1900334. https://doi.org/10.1002/aenm.201900334.